Article

Not peer-reviewed version

Structural and Optical Characterization of Porous NiV2O6 Films Synthesized by Nebulizer Spray Pyrolysis for Photodetector Applications

Ahmed Kotbi , Islam Radaf , Ilham Hamdi Alaoui , Anna Cantaluppi , Andreas Zeinert , Abdelilah LAHMAR *

Posted Date: 18 March 2024

doi: 10.20944/preprints202403.1014.v1

Keywords: NiV2O6 thin films; Porous microstructure; Absorption coefficient; Energy gap; Photodetector

Article

Structural and Optical Characterization of Porous NiV_2O_6 Films Synthesized by Nebulizer Spray Pyrolysis for Photodetector Applications

Ahmed Kotbi [1], Islam Radaf [2,3], Ilham Hamdi Alaoui [1], Anna Cantaluppi [1], Andreas Zeinert [1] and Abdelilah Lahmar [1,*]

[1] Laboratory of condensed Matter Physics, University of Picardie Jules Verne, 33 Rue Saint Leu, 80039 Amiens, France
[2] Electron Microscope and Thin Films Department, Physics Research Institute, National Research Centre, 33 El Bohoos Str., Dokki, Giza 12622, Egypt
[3] Department of Physics, College of Science and Arts at ArRass - Qassim University, ArRass 51921, Saudi Arabia
* Correspondence: abdel.ilah.lahmar@u-picardie.fr; Tel.: +33-3-22-82-76-91

Abstract: NiV_2O_6 thin films were grown on glass slides with varying thicknesses using the nebulizer spray pyrolysis. The impact of thickness on the thin films' optical, structural, morphological, and electrical characteristics was systematically investigated. The X-ray diffraction and micro-Raman analysis confirmed the formation of the triclinic NiV_2O_6 system. Surface morphology and roughness variations in the as-deposited NiV_2O_6 films were studied using scanning electron microscopy (SEM) and a profilometer. Optical properties, including optical band gap (Eg), extinction coefficient (k), absorption coefficient (α), and refractive index (n), were determined through optical reflectance and transmittance measurements. The optical energy gap of the as-deposited NiV2O6 films decreased from 2.3 eV to 1.9 eV with increased layer thickness. Furthermore, the photo-detectivity of the films demonstrated an enhancement corresponding to the prolonged spray time. The sensitivity values obtained for visible irradiation are 328, 511, and 433 for samples S1, S2, and S3, respectively. The obtained results are imputed to the specific porous microstructure.

Keywords: NiV_2O_6 thin films; Porous microstructure; absorption coefficient; energy gap; photodetector

1. Introduction

Recently, much attention has been directed to metal oxide thin films due to their remarkable and captivating optical, optoelectronic, and electrical characteristics. These metal oxides exhibit exceptional thermal stability and possess a significant absorption coefficient. The distinctive characteristics of these metal oxides render them well-suited for various applications, such as optical memory devices, window layers for solar cells, IR sensors, and photodetectors. Photodetection converts light into an electrical signal, which is crucial in many modern technologies [1].

Among the widely used materials for photodetection are semiconductors such as silicon [2], III-V compounds like gallium arsenide [3], and other materials based on nanomaterials, including graphene [4–8], 2D transition metal dichalcogenides (TMDCs) [9], and graphitic-carbon nitride (g-C3N4) [10,11]. Graphene was the initial 2D material explored for photodetectors, capitalizing on its remarkable electrical characteristics, notably its impressive carrier mobility [6,7] and a high-speed bandwidth of up to 40 GHz [5–7]. However, the absence of a bandgap in graphene results in dark currents, contributing significantly to signal noise. This limitation substantially restricts its broader applications in photodetection. Among TMDs, molybdenum disulfide (MoS_2) has attracted much interest in the last decade due to its high mobility, high optical absorption capacity and tunable

 doi:10.20944/preprints202403.1014.v1

bandgap [12–14]. These materials have specific properties that make them suitable for various wavelength ranges and diverse applications, ranging from detecting low light levels to high-speed optical communication. Exploring the properties of these materials opens up exciting possibilities for enhancing photodetection performance and expanding its applications in areas such as remote sensing, medicine, and quantum technology.

The use of advanced materials in developing optoelectronic devices, such as photodetectors, has become crucial to meet increasing performance requirements. A new material, NiV_2O_6, a compound of nickel and vanadium, emerges as a promising candidate for photodetection applications due to its inimitable properties. NiV_2O_6 has intrinsic characteristics that make it an attractive material, including its tunable optoelectronic properties. The ease of large-scale manufacturing of NiV_2O_6, its wide band gap of 2.4 eV [15,16], sensitive optical responses, high absorption coefficient exceeding 10^6 m^{-1}, and its porous structure make it an attractive material for various applications.

For instance, light trapping technique approach has widely used as an appropriate way to improve the efficiency of the solar cell using generally the Silicon bottom texturing or a transparent conductor in the superstrate-type cells, compared to non-porous structures [17]. Further, the high efficiency photoelectrochemical water splitting was reported for porous TiO_2, almost two times than that of the photoanode formed by TiO_2 nanoparticle-based films (P25) [18].

In the present work, we emphasize the fundamental properties of porous NiV_2O_6 film, its synthesis process, and its potential as a light-sensitive material for photodetectors, providing insight into its possibilities in optical sensing.

2. Materials and Methods

This work used a spray pyrolysis process to fabricate NiV_2O_6 layers. The precursor solution is produced from the chemical reaction between two solutions. We added 40 ml of 0.1 M nickel nitrate $Ni(NO3)_2$ to 60 ml of 0.2 M of ammonium vanadate NH_4VO_3. The mixture was stirred for 15 minutes. The heated glass slides were sprayed with the NiV_2O_6 solution for 4, 6, and 9 minutes. The spray pyrolysis settings were adjusted at the substrate temperature of 250 °C, 5 ml/min for the flow rate, and 3 atm for the air pressure. The distance between the nozzle and the substrate has been adjusted to 30 cm. Using the Bruker-Dektak stylus profiler, the thickness of the NiV_2O_6 layers has been measured (S1 is 0.86 μm, S2 is 2.41 μm, and S3 is 2.94 μm). The structural analysis of the phase formation was detected by X-ray diffraction (XRD) type a four-circle Bruker Discover D8 diffractometer with CuKα = 1.5406 Å (D8 Advance, Bruker, Germany). The vibrational analyses were recorded with a micro-Raman Renishaw spectrometer using a green laser excitation source (532 nm). The microstructure and the composition of the NiV_2O_6 films were investigated by a scanning electron microscope (SEM) Quanta 200 FEG equipped with energy-dispersive X-ray spectroscopy (EDX). The optical properties were analyzed using a JASCO V- 670 UV-vis-near IR spectrometer. The thickness and roughness of the films were determined by the Bruker profilometer (model: Dektak XT). The photo-response of the deposited samples is characterized under a 1.5 G AM spectrum of an Ossila solar simulator (model No. G2009A1) at a constant applied bias of 3V using Palmsens 4 electrical measurements station by two probe method at room temperature.

3. Results and Discussion

3.1. Microstructural and Surface Morphology Study

The microstructural characteristics of the prepared NiV_2O_6 films were examined by scanning electron microscope, as shown in Figure 1. SEM images reveal complex and heterogeneous three-dimensional surfaces featuring irregularly dispersed pores of varying sizes and shapes. Image (a) of sample S1 exhibits the texture of a dense and porous structure with predominantly superficial pores. In contrast, images (b and c) of samples S1 and S2 depict deeper pores, resulting in significantly larger specific surface areas.

 doi:10.20944/preprints202403.1014.v1

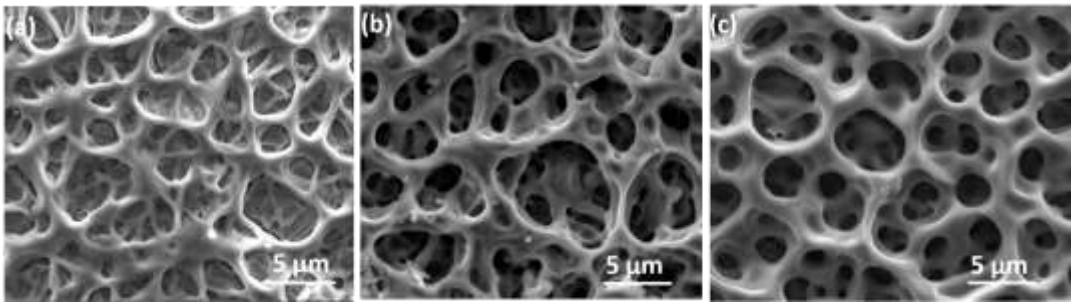

Figure 1. SEM images showing the microstructure of the investigated thin films.

The porous and meshing structure of NiV_2O_6 makes it an attractive material for various applications such as photodetection and gas sensors, which will benefit from a large specific surface area. Moreover, the EDX spectra of the elaborated samples are illustrated in Figure 2. The EDX spectra displayed the existence of Ni, V, and O peaks in all samples, and their atomic ratios are 1:2: 6, respectively.

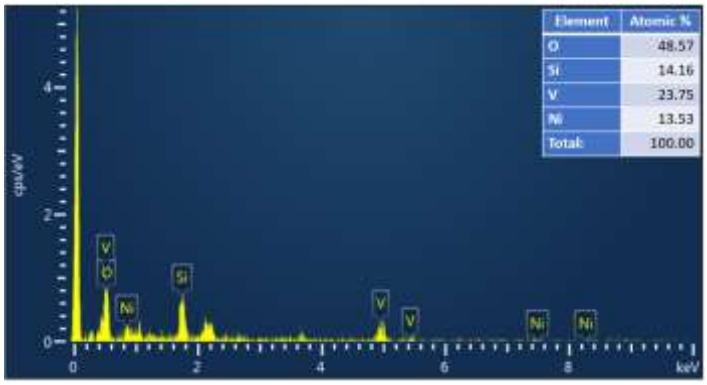

Figure 2. Example of EDX spectra with the atomic percentage of a NiV_2O_6 thin film.

On the other hand, the roughness and surface morphology of the NiV_2O_6 films were assessed through mapping using a profilometer. Figures 3a–c present 3D micrographs of NiV_2O_6 thin films captured in a scanning area of (0.5 × 0.5) mm2. These images clearly illustrate the correlation between surface roughness and film thickness. It is noted that the surface roughness escalates as the film thickness increases. Specifically, the average film roughness increases from 0.26 µm to 0.49 µm as the film thickness increases. This trend will increase the quantity of trapped light and, therefore, the light-material reaction, i.e., the absorption for the very thick samples S2 and S3.

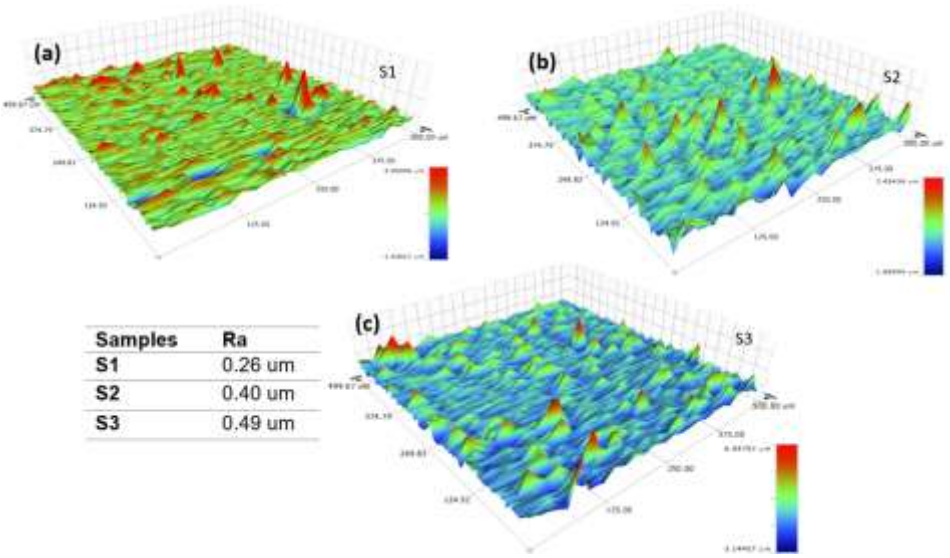

 doi:10.20944/preprints202403.1014.v1

Figure 3. Profilometer mapping of thin layers of NiV_2O_6.

3.2. Structural Investigation

Figure 4 depicts the XRD of the NiV_2O_6 thin films, in the limit of detection device. The figure displays only four distinguished diffraction patterns. According to the Standard JCPDS file no. 76-0359, the observed peaks might be indexed with (211), (002), (322), and (340) planes of the NiV_2O_6 single triclinic structure. Complementary structural information is needed to confirm this assumption

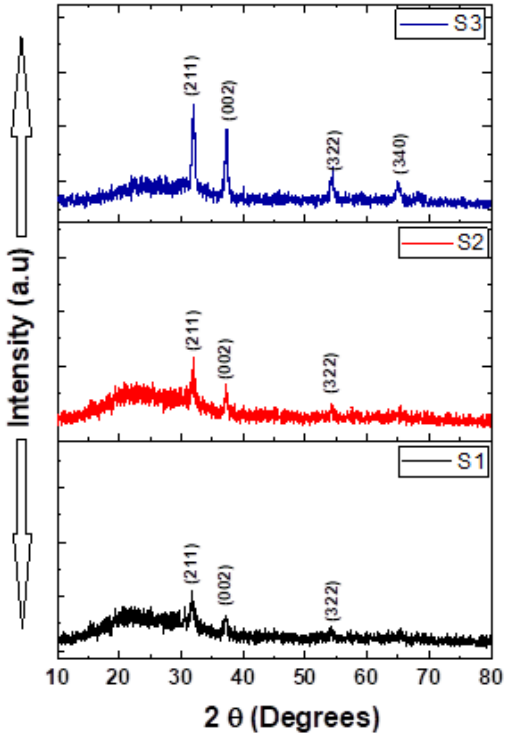

Figure 4. X-ray diffraction patterns of the porous NiV_2O_6 films.

Raman spectroscopy is an effective tool for investigating structural and bonding characteristics, providing valuable insights into materials' local structure, crystallization and electronic properties. The Raman bands of NiV_2O_6 in the 100-900 cm^{-1} range were obtained with varying spray times, as depicted in Figure 5.

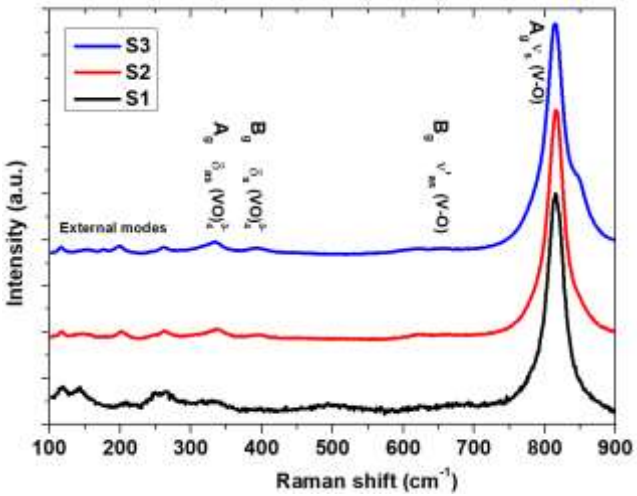

Figure 5. Raman spectra of the investigated NiV_2O_6 films.

 doi:10.20944/preprints202403.1014.v1

Consistent Raman bands at 327, 367, 647, and 816 cm^{-1} were observed across all samples, indicative of the distinctive vibrational bands of the triclinic NiV_2O_6 system. A comparison of vibration modes for different materials like NiV_2O_6 is summarized in Table 1. The prominent band at 816 cm^{-1} corresponds to the shorter symmetric V–O stretching mode (Ag), while the weaker band at 647 cm^{-1} is associated to the short (Bg) asymmetric V–O stretching modes [19]. Additionally, the asymmetric and symmetric bending vibrations of the VO_4 tetrahedron were identified at 327 and 367 cm^{-1}, respectively [20]. Alternatively, within our sample S3, we detected a shoulder at 846 cm^{-1}, which can be ascribed to a division arising from the lower symmetry of the monoclinic structure [21]. The vibrations of the crystal lattice (external modes) are responsible for the peaks observed at 138 and 205 cm^{-1} [22].

Table 1. Vibrational modes observed in Raman spectrum for different materials like NiV_2O_6.

Materials	Assignment	Raman shift (cm^{-1})
CoV_2O_6	$_{S}$V-O-V	775 [19]
	$_{as}$V-O	851 [19]
	$_{as}$V-O	913 [19]
	$_{S}$V-O	946 [19]
$Li_{0.8}NiVO_4$	δ_{as} (VO_4)	332 [23]
	ν_{as} (V-O)	795 [23]
	ν_s (V-O)	825 [23]
Cu–$BiVO_4$	External modes	210 [21]
	δ_{as} (VO_4)	327 [21]
	δ_s (VO_4)	367 [21]
	ν'_{as} (V-O)	637 [21]
	ν_{as} (V-O)	710 [21]
	ν_s (V-O)	819 [21]
$BiVO_4$	δ_{as} (VO_4)	324 [20]
	δ_s (VO_4)	367 [20]
	ν_{as} (V-O)	710 [20]
	ν_s (V-O)	811 [20]
Mo–$BiVO_4$	External modes	213 [24]
	δ_{as} (VO_4)	327 [24]
	δ_s (VO_4)	367 [24]
	ν'_{as} (V-O)	642 [24]
	ν_{as} (V-O)	710 [24]
	ν_s (V-O)	831 [24]
$BiVO_4$	External modes	27, 211 [22]
	δ_{as} (VO_4)	324 [22]
	δ_s (VO_4)	368 [22]
	ν_{as} (V-O)	703 [22]
	ν_s (V-O)	828 [22]
NiV_2O_6	External modes	138, 205 (This work)
	δ_{as} (VO_4)	327 (This work)

 doi:10.20944/preprints202403.1014.v1

	δ_s (VO_4)	367 (This work)
	ν'_{as} (V-O)	647 (This work)
	ν_s (V-O)	816 (This work)

3.3. Optical Study

The absorption coefficient (α) was determined using the formula [25]:

$$\alpha = \frac{1}{d}\ln\left(\frac{(1-R)^2}{T}\right) \quad (1)$$

where d represents the film thickness, T signifies transmittance, and R is the reflectance of the samples. The optical bandgap energy (Eg) was derived from the absorption coefficient (α) through the application of the Tauc model. [26,27]:

$$\alpha h\vartheta = A(h\vartheta - E_g)^m \quad (2)$$

where $h\vartheta$ represents the photon energy, A is a constant, Eg is the optical band gap, and n is an exponent indicating the nature of optical absorption. For a direct authorized transition, m = 1/2; for an indirect authorized transition, m = 2; for a direct forbidden transition, m = 3/2; and for an indirect forbidden transition, m = 3. The bandgap energy (Eg) of the developed NiV_2O_6 is obtained by plotting $(\alpha h\nu)^2$ versus photon energy (Figure 6b)

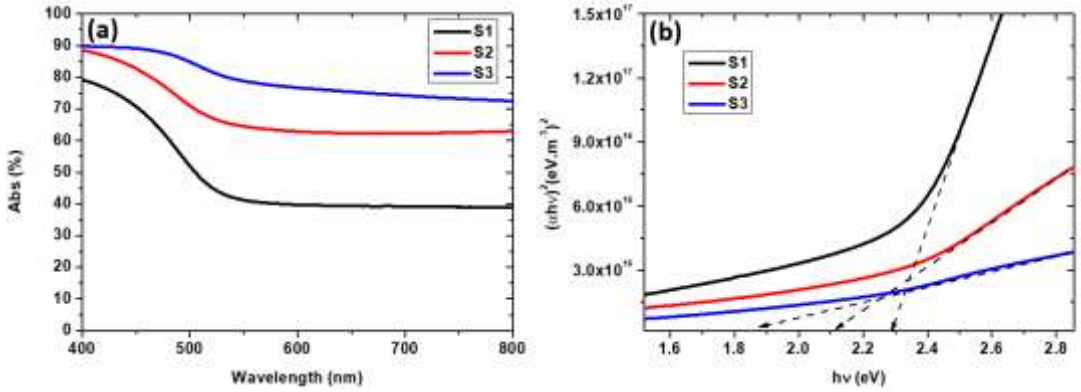

Figure 6. (a) Absorptance spectra of NiV_2O_6 films synthesized at different thicknesses; (b) A Tauc plot for a NiV_2O_6 fabricated thin film.

The dielectric function $\varepsilon(\omega)$ is a critical factor for the optical properties of a semiconductor, which could be defined by the below (3) [28,29]:

$$\varepsilon(\omega) = \varepsilon_1(\omega) - i\varepsilon_2(\omega) \quad (3)$$

where $\varepsilon_1(\omega)$ is the real part of the dielectric function, and $\varepsilon_2(\omega)$ is the imaginary parts of the dielectric functions, which can represent electronic transitions linked to conduction and valence bands.

The refractive index is a characteristic of a medium, describing the behavior of light in it, whose complex form $n^* = n - ik$ [28], where n represents the refractive index, and k refers to the extinction coefficient calculated by the following equation k= $\alpha\lambda/4\boldsymbol{\pi}$. The variations of the absorption coefficient α, the extinction coefficient k and the refractive index n as a function of wavelength are given in Figure 7a–c. These parameters inform us about the loss of energy in the medium, i.e., the absorption of the photons. NiV_2O_6 is a promising material for fabricating photodetector devices due to its wide optical bandgap energy of 2.3 eV, and its high optical absorption coefficient > 10^6 m^{-1} [30]. It is important to emphasize that the porous structure of our samples leads to optical data relative to this effective medium (NiV_2O_6 + the pores). These datado notuniquely refer to the NiV_2O_6 phase of

Preprints.org (www.preprints.org) | NOT PEER-REVIEWED | Posted: 18 March 2024 doi:10.20944/preprints202403.1014.v1

the spongy material. It is well known that NiV_2O_6 is a semi-conductor and one therefore expects a very low absorption for energies below the bandgap, in contrast to what can be observed in our samples where the absorbed energy is higher than 40% for the longer wavelengths. This is owed to the highly porous structure of the material. As the sample S1 exhibits a higher density and a less spongy structure than the other two samples its band gap is near to that one expected for the NiV_2SO_6, while for S2 and S3 the lower bandgaps just reflect their more porous microstructure. This is underlined by the very high energy fraction absorbed even at higher wavelengths for these samples. Therefore, this relative decrease of Eg does not mean that the electronic structure of the NiV_2SO_6 phase has changed (there is no quantum confinement for instance) for S2 and in S3.

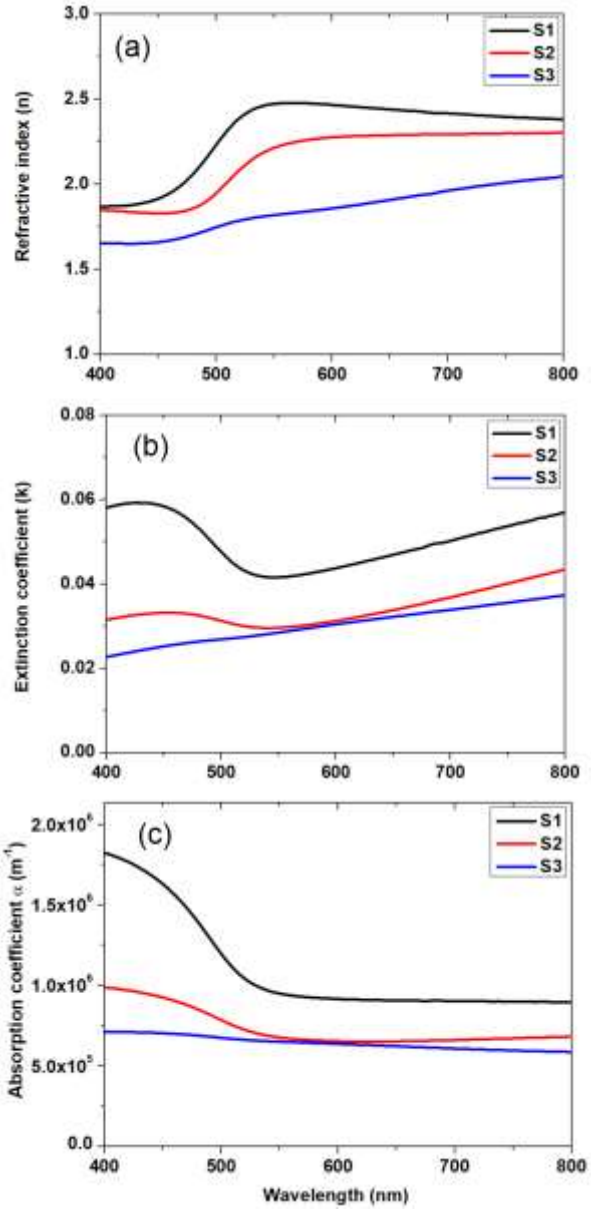

Figure 7. (a) The variation of n of the NiV_2O_6 films versus λ, (b) The extinction coefficient of the NiV_2O_6 films versus λ and (c) The absorption coefficient of the NiV_2O_6 films versus λ.

3.4. Photodetector Application

In this work, the sensitivity was studied with different film thicknesses at constant light source intensity (100 mW/cm²) and effective illumination area (0.1 cm²) (Figure 8). The sensitivity depends on the intensity of the light source and the effective illumination area. The photodetector's performance is evaluated by a key parameter known as sensitivity (S), which can be defined as [30]:

 doi:10.20944/preprints202403.1014.v1

$$S(\%) = \frac{I_{ph}}{I_{dark}} \times 100 \quad (4)$$

where Iph is the photocurrent, and it is equal I_{light} - I_{dark}, moreover, I_{dark} is the dark current, and I_{light} is the light current. At a bias voltage of 3V, the sensitivity values for samples S1, S2, and S3 were computed and found to be around 328, 511, and 433, respectively, as presented in Table 2. It is observed that the sensitivity of the layers increases with the boost in layer thickness due to the increase in the optical absorption of the films.

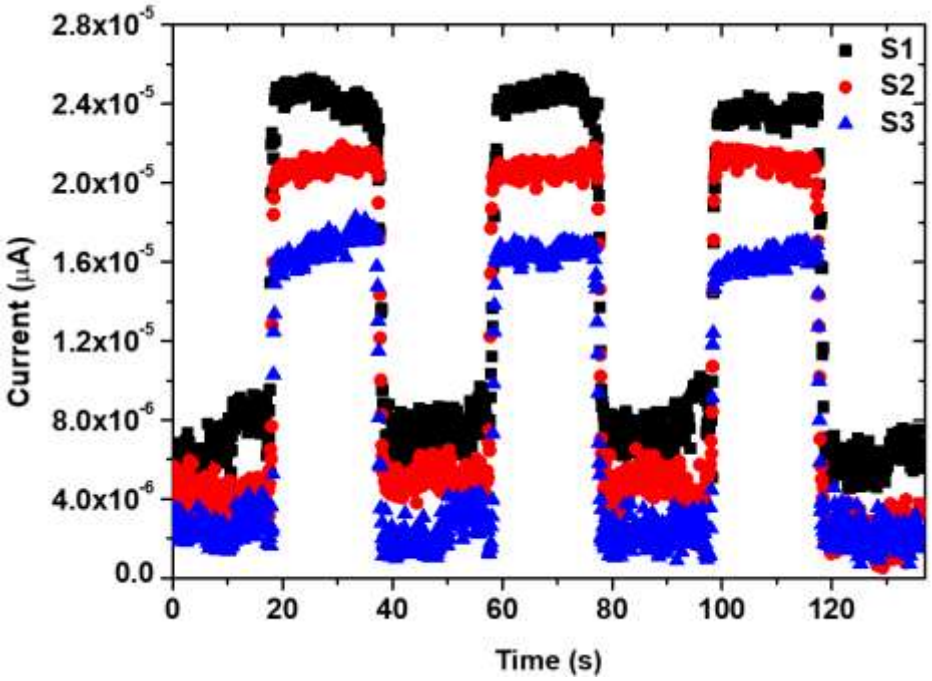

Figure 8. J-t characteristics of NiV_2O_6 films below chopped AM 1.5 (100 mW.cm^{-2}) lighting.

Table 2. Photodetector performance compared with those reported by others.

Samples	Rise time (s)	Decay time (s)	Sensitivity (%)	Ref.
S1	0.62	1.19	328	This work
S2	0.29	0.52	511	This work
S3	0.43	0.69	433	This work
Fe-doped ZnO/$BiVO_4$	0.17	-	2900	[31]
SnS	0.44	0.50	697	[32]
GaTe	0.045	0.045	788	[33]
MoSe2	0.4	0.2	1626	[34]

Rise and decay times are crucial parameters in assessing photodetector performance. For a single on/off cycle, the rise times were determined to be approximately 0.62, 0.29, and 0.43 seconds. In contrast, decay times were found to be 1.19, 0.52, and 0.69 seconds at a bias voltage of 3 V for samples S1, S2, and S3, respectively (Figure 9). Sample S2 exhibited very fast rise and decay times, as revealed by the photo-response time results

 doi:10.20944/preprints202403.1014.v1

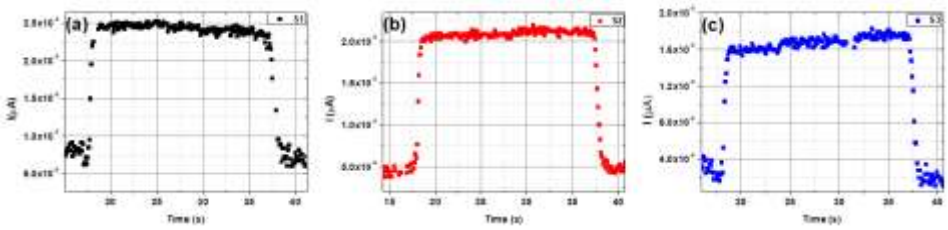

Figure 9. Rise and decay time under 3 V bias voltage for the investigated samples.

4. Conclusions

This research involved the successful fabrication of NiV_2O_6 thin films on glass substrates through the application of the spray pyrolysis technique. The influence of spray time on the optical properties of NiV_2O_6 films has been investigated. A triclinic structure was obtained for all samples. The reflectance and transmission spectra are utilized to compute the optical constants, including the refractive index (n) and extinction coefficient (k). With increased film thickness, the effective band gap value decreases from 2.3 eV to 1.9 eV. The film's photo response parameters, like sensitivity (S), increase with film thickness. The fastest rise and fall times of 0.29 s and 0.52 s were obtained for sample S2.

However, it is interesting to point out herein that the properties obtained are not intrinsic to the films alone. The specific microstructure in which the pores take place, and change depth with increasing thickness, plays a key role in trapping light and changing the behavior that would be observed if the microstructure of the films were continuous and smooth. The versatile method used herein for processing films with high active area is promising for a wide range of applications.

Author Contributions: Conceptualization, A.L. and I.M.E; validation, A.L., A.Z.; formal analysis, A.K.; investigation, A.K., I.H.A and A.C.; data curation, A.K. and I.M.E; visualization, I.H.A and A.C.; writing—original draft preparation, A.K.; writing—review and editing, A.L, A.Z and I.M.E, supervision, A.Z.; All authors have read and agreed to the published version of the manuscript.

Funding: This work was supported by PARS (ANR-DFG) project N°22003

Data Availability Statement: Not applicable.

Conflicts of Interest: The authors declare no conflict of interest.

References

1. Banerjee, D.; Chattopadhyay, K.K. Chapter 5 - Hybrid Inorganic Organic Perovskites: A Low-Cost-Efficient Optoelectronic Material. In; Thomas, S., Thankappan, A.B.T.-P.P., Eds.; Academic Press, 2018; pp. 123–162 ISBN 978-0-12-812915-9.
2. Piels, M.; Bowers, J.E. 1 - Photodetectors for silicon photonic integrated circuits. In; Nabet, B.B.T.-P., Ed.; Woodhead Publishing, 2016; pp. 3–20 ISBN 978-1-78242-445-1.
3. Channel, E.T. Fast Response GaAs Photodetector Based on Constructing Electron Transmission Channel. 2021, 1–8.
4. Kotbi, A.; Imran, M.; Kaja, K.; Rahaman, A.; Ressami, E.M.; Lejeune, M.; Lakssir, B.; Jouiad, M. Graphene and g-C3N4-Based Gas Sensors. J. Nanotechnol. 2022, 2022, 9671619, doi:10.1155/2022/9671619.
5. Chen, X.; Shehzad, K.; Gao, L.; Long, M.; Guo, H.; Qin, S.; Wang, X.; Wang, F.; Shi, Y.; Hu, W.; et al. Graphene Hybrid Structures for Integrated and Flexible Optoelectronics. Adv. Mater. 2020, 32, 1902039, doi:https://doi.org/10.1002/adma.201902039.
6. Vicarelli, L.; Vitiello, M.S.; Coquillat, D.; Lombardo, A.; Ferrari, A.C.; Knap, W.; Polini, M.; Pellegrini, V.; Tredicucci, A. Graphene field-effect transistors as room-temperature terahertz detectors. Nat. Mater. 2012, 11, 865–871, doi:10.1038/nmat3417.
7. Schuler, S.; Muench, J.E.; Ruocco, A.; Balci, O.; Thourhout, D. van; Sorianello, V.; Romagnoli, M.; Watanabe, K.; Taniguchi, T.; Goykhman, I.; et al. High-responsivity graphene photodetectors integrated on silicon microring resonators. Nat. Commun. 2021, 12, 3733, doi:10.1038/s41467-021-23436-x.
8. Guo, X.; Wang, W.; Nan, H.; Yu, Y.; Jiang, J.; Zhao, W.; Li, J.; Zafar, Z.; Xiang, N.; Ni, Z.; et al. High-performance graphene photodetector using interfacial gating. Optica 2016, 3, 1066–1070, doi:10.1364/OPTICA.3.001066.

9. Li, Y.; Li, L.; Li, S.; Sun, J.; Fang, Y.; Deng, T. Highly Sensitive Photodetectors Based on Monolayer MoS2 Field-Effect Transistors. ACS Omega 2022, 7, 13615–13621, doi:10.1021/acsomega.1c07117.
10. Kotbi, A.; Benyoussef, M.; Ressami, E.M.; Lejeune, M.; Lakssir, B.; Jouiad, M.; Hills, V. Gas Sensors Based on Exfoliated g-C 3 N 4 for CO 2 Detection. 2022.
11. Fang, H.; Ma, H.; Zheng, C.; Lennon, S.; Wu, W.; Wu, L.; Wang, H. A high-performance transparent photodetector via building hierarchical g-C3N4 nanosheets/CNTs van der Waals heterojunctions by a facile and scalable approach. Appl. Surf. Sci. 2020, 529, 147122, doi:https://doi.org/10.1016/j.apsusc.2020.147122.
12. Mouloua, D.; Kotbi, A.; Deokar, G.; Kaja, K.; El Marssi, M.; EL Khakani, M.A.; Jouiad, M. Recent Progress in the Synthesis of MoS2 Thin Films for Sensing, Photovoltaic and Plasmonic Applications: A Review. Materials (Basel). 2021, 14, 3283, doi:10.3390/ma14123283.
13. Nasr, M.; Benhamou, L.; Kotbi, A.; Rajput, N.S.; Campos, A.; Lahmar, A.I.; Hoummada, K.; Kaja, K.; El Marssi, M.; Jouiad, M. Photoelectrochemical Enhancement of Graphene@WS2 Nanosheets for Water Splitting Reaction. Nanomaterials 2022, 12, doi:10.3390/nano12111914.
14. Matras, G.; Marssi, M. El; Kotbi, A. MoS 2 Based Nanomaterial for Light Emitting Diode Applications. 2022 Adv. Sci. Eng. Technol. Int. Conf. 1–5, doi:10.1109/ASET53988.2022.9734931.
15. Rahman, M.A.; Akter, M.R.; Khatun, M.R.; Sultana, R.; Sarker, M.A.R. Synthesis and Characterization of High-Quality Polycrystalline Sample NiV 2 O 6 by Solid-State Reaction Technique. 2020, 62, 1024–1032, doi:10.1134/S1063783420060049.
16. Dang, H.X.; Rettie, A.J.E.; Mullins, C.B. Visible-Light-Active NiV 2 O 6 Films for Photoelectrochemical Water Oxidation. 2015.
17. A.F.A. Rahim, M.A. Ahmed, N.S.M. Razali, R. Radzali, A. Mahmood, I.H. Hamzah and E. Noorsal, Investigation of Light Trapping from Porous Silicon Surface for the Enhancement of Silicon Solar Cell Performance,Acta Physica Polonica A, 2019, 135, 637-642
18. Yuanxing Fang, Ronan Hodgson, Wei Cheat Lee, Huyen Le, Hon Wing Boaz Chan, Hassan M. Hassan, Ibrahim H. Alsohaimi,Giacomo E. Canciani, Rong Qian and Qiao Chen,Light trapping by porous TiO2 hollow hemispheres for high efficiency photoelectrochemical water splitting,: Phys. Chem. Chem. Phys.2023, 25, 11253,DOI: 10.1039/d2cp04246k.
19. Pereira, R.; Rodrigues, A.D.; Pereira, E.C.; Oliveira, A.J.A. De Sol-gel synthesis of triclinic CoV 2 O 6 polycrystals. Ceram. Int. 2018, 44, 19397–19401, doi:10.1016/j.ceramint.2018.07.171.
20. Helal, A.; El-sheikh, S.M.; Yu, J. Novel synthesis of BiVO 4 using homogeneous precipitation and its enhanced photocatalytic activity. 2020.
21. Merupo, V.; Velumani, S.; Ordon, K.; Errien, N.; Szade, J.; Kassiba, A. Structural and optical characterization of ball-milled copper-doped bismuth vanadium oxide (BiVO4). CrystEngComm 2015, doi:10.1039/C5CE00173K.
22. Properties, P. Aerosol-Assisted CVD of Bismuth Vanadate Thin Films and Their Aerosol-Assisted CVD of Bismuth Vanadate Thin Films and Their Photoelectrochemical Properties. 2015, doi:10.1002/cvde.201407142.
23. Bhuvaneswari, M.S.; Selvasekarapandian, S.; Kamishima, O. Vibrational analysis of lithium nickel vanadate. 2005, 139, 279–283, doi:10.1016/j.jpowsour.2004.07.006.
24. Merupo, V.I.; Velumani, S. Structural and Optical properties of Molybdenum doped Bismuth vanadate powders. 2014, 0–4, doi:10.1109/ICEEE.2014.6978299.
25. Kotbi, A.; Hartiti, B.; Ridah, A.; Thevenin, P. Characteristics of CuInS2 thin films synthesizes by chemical spray pyrolysis. Opt. Quantum Electron. 2016, 48, 1–9, doi:10.1007/s11082-015-0344-6.
26. Zhang, S.; Zhang, J.Z.; Han, M.J.; Li, Y.W.; Hu, Z.G.; Chu, J.H. Temperature dependent near infrared ultraviolet range dielectric functions of nanocrystalline (Na0.5Bi0.5)1-xCex(Ti0.99Fe0.01)O3 films. Appl. Phys. Lett. 2014, 104, 0–5, doi:10.1063/1.4863417.
27. Kotbi, A.; Hartiti, B.; Fadili, S.; Ridah, A.; Thevenin, P. Experimental and theoretical studies of CuInS2 thin films for photovoltaic applications. J. Mater. Sci. Mater. Electron. 2019, doi:10.1007/s10854-019-02479-3.
28. Zhang, H.; Tang, Y.; Liu, Z.; Zhu, Z.; Tang, X.; Wang, Y. Study on optical properties of alkali metal doped g-C3N4 and their photocatalytic activity for reduction of CO2. Chem. Phys. Lett. 2020, 751, 137467, doi:10.1016/j.cplett.2020.137467.
29. Kotbi, A.; Hartiti, B.; Fadili, S.; Ridah, A.; Thevenin, P. Experimental and theoretical studies of CuInS2 thin films for photovoltaic applications. J. Mater. Sci. Mater. Electron. 2019, 30, 21096–21105, doi:10.1007/s10854-019-02479-3.
30. Gupta, Y.; Arun, P. Suitability of SnS thin films for photovoltaic application due to the existence of persistent photocurrent. Phys. status solidi 2016, 253, 509–514, doi:https://doi.org/10.1002/pssb.201552249.
31. Veeralingam, S.; Yadav, P.; Badhulika, S. An Fe-doped ZnO/BiVO4 heterostructure-based large area, flexible, high-performance broadband photodetector with an ultrahigh quantum yield. 2020, 9152–9161, doi:10.1039/c9nr10776b.

 doi:10.20944/preprints202403.1014.v1

32. Mahdi, M.S.; Ibrahim, K.; Hmood, A.; Ahmed, N.M.; Mustafa, F.I.; Azzez, S.A. High performance near infrared photodetector based on cubic crystal structure SnS thin film on a glass substrate. Mater. Lett. 2017, 200, 10–13, doi:10.1016/j.matlet.2017.04.077.
33. Wang, Z.; Safdar, M.; Mirza, M.; Xu, K.; Wang, Q.; Huang, Y.; Wang, F.; Zhan, X.; He, J. High-performance flexible photodetectors based on GaTe nanosheets. Nanoscale 2015, 7, 7252–7258, doi:10.1039/C4NR07313D.
34. Jung, C.; Kim, S.M.; Moon, H.; Han, G.; Kwon, J.; Hong, Y.K.; Omkaram, I.; Yoon, Y.; Kim, S.; Park, J. Highly Crystalline CVD-grown Multilayer MoSe2 Thin Film Transistor for Fast Photodetector. Sci. Rep. 2015, 5, 15313, doi:10.1038/srep15313.